Comparison of Langmuir probe and laser Thomson scattering for electron property measurements in magnetron discharges

Peter J. Ryan,[a] James W. Bradley, and Mark D. Bowden
Department of Electrical Engineering and Electronics, University of Liverpool, Brownlow Hill, Liverpool L69 3GJ, United Kingdom

(Dated: 19 August 2019)

Electron property measurements made by Langmuir probe and laser Thomson scattering have been compared in weakly magnetized plasma conditions using a planar unbalanced magnetron with the aim of assessing the accuracy of the probe diagnostic. Measurements were performed at several locations within the magnetic field configuration; the magnetic null region ($\lesssim 1$ mT) on the discharge axis and inside the last closed flux surface boundary with fields up to 33 mT. There was good diagnostic agreement during High Power Impulse Magnetron Sputtering (HiPIMS) but significant discrepancies were observed for DC magnetron operation, even at the magnetic null. For some discharge conditions, the electron density determined by Thomson scattering was over an order of magnitude greater than the plasma density obtained from the Langmuir probe, using both ion and electron collection theories. In addition, the low energy part of the electron energy distribution function determined by the probe was depleted. The possible reasons for the discrepancies are discussed, with the conclusion being that the plasma was significantly perturbed by the probe stem. The range of plasma density and electron temperature measured in the study were 0.4-54 $\times 10^{17}$ m^{-3} and 0.2-5.9 eV, respectively.

I. INTRODUCTION

Electrons are the driving force of many physical and chemical processes in low temperature plasma devices. Knowledge of the electron energy distribution function (EEDF) is essential for any discharge physics investigation because it determines the types of interaction a heavy species can have with an electron (e.g. elastic and inelastic collisions) and the frequency at which they occur. For the case of a Maxwellian distribution of electrons, the EEDF is characterized by electron density (n_e) and temperature (T_e). For many conditions/discharges, however, the EEDF is non-Maxwellian and so its shape must be measured.

Langmuir probes are routinely used for electron property measurements in both Maxwellian and non-Maxwellian[1] plasmas. The current-voltage (IV) characteristic from a single Langmuir probe is relatively simple to measure, moreover, it contains a wealth of localized information, which can be used to calculate several plasma parameters by implementing a suitable probe theory[2,3]: n_e, T_e, EEDF, ion density (n_i), plasma potential (V_p) and floating potential (V_f). The main limitations are that the probe is intrusive and a probe theory is selected based on the plasma properties a priori to the data analysis.

One of the most challenging operating regimes of the Langmuir probe is in magnetized plasma because it is difficult to model the transport anisotropy caused by the magnetic field impeding cross-field transport[2]. Furthermore, the probe has a longer disturbance length scale compared to operation in an unmagnetized plasma because the charge collected by the probe is replenished at a slower rate[4]. In these conditions, the probe current is reduced and is dependent on several parameters: the probe tip size with respect to the ion and electron gyroradii (r_{gi}, r_{ge} for ions and electrons, respectively)[5,6] and Debye length (λ_D); the probe tip orientation with respect to the B-field[5,7]; chamber size/geometry[8]; collisionality[2,3]; plasma instabilities; and the applied voltage with respect to V_p. Some of these factors are unique to each discharge and a complete probe theory has never been developed. An experimentalist, therefore, often has to use unmagnetized probe theories. This may result in a relatively large uncertainty for locating V_p due to rounding of the IV curve knee[9]; distortion of the measured EEDF, especially the low energy part[6]; plasma density underestimation[6,10,11]; and T_e overestimation[12].

Technological plasma devices generally use weak magnetic fields ($B < 100$ mT), as a result, electrons are the only magnetized species in the plasma. Experimental effort is required to demonstrate the error caused by using unmagnetized electron probe theories in these conditions in order to understand the limitations of the diagnostic. Previous studies have used the probe determined n_i as the benchmark to compare with n_e[6,10], despite the ion current collected by the probe being strongly influenced by collisions with the background gas[9,13,14]. Therefore, the choice of probe theory for calculating n_i is crucial, and so, the benchmark density cannot be considered reliable. In addition, the accuracy of T_e measurements using a probe in weakly magnetized conditions remains to be verified. A probe comparison study using an accurate independent diagnostic is required.

In this article, we compare the Langmuir probe and laser incoherent Thomson scattering diagnostics in weakly magnetized plasma in order to assess the accuracy of the Langmuir probe for electron property measurements (n_e, T_e and EEDF). The advantages of using Thomson scattering as the reference diagnostic are that it has simple data interpretation, which is independent of magnetic field strength, because the shape of the scattering spectrum is proportional to the electron velocity distribution function (EVDF) in the incoherent regime[15]; the calibration procedure for absolute electron density values is straightforward; it is non-intrusive; and it has

[a]Electronic mail: ryanp@liverpool.ac.uk

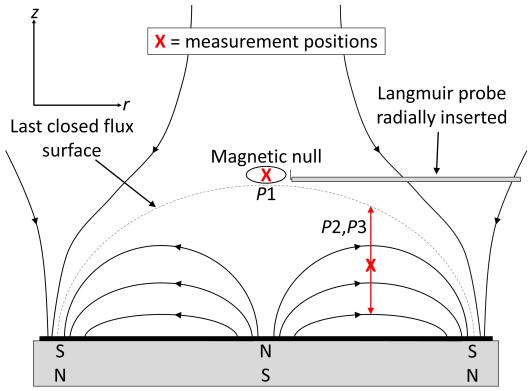

FIG. 1. Schematic of the magnetic field from an unbalanced planar magnetron. In this study the tungsten target diameter was 150 mm and the measurement positions were at the magnetic null ($r = 0$ mm, $z = 61$ mm), labeled as $P1$, and at a single radial position inside the last closed flux surface boundary ($r = 41$ mm, $z = 10-50$ mm), labeled as $P2$ and $P3$. The azimuth locations of $P2$ and $P3$ are shown in figure 2(a). The system origin ($r = 0$ mm, $z = 0$ mm) is located at the center of the target surface. For reference, the main racetrack erosion is at ($r = 48$ mm, $z = 0$ mm).

good spatial resolution. Other standard non-intrusive diagnostics, such as microwave interferometry[16] and optical emission spectroscopy[17], are unable to provide the same unambiguous measurements of localized n_e, T_e and EEDF. The disadvantages of Thomson scattering are that a complex, expensive experimental setup is required and the measurements are insensitive to the tail of the EVDF. Previous comparison studies of Langmuir probes and Thomson scattering found relatively good agreement[18–22], but there has not been a detailed study in weakly magnetized conditions.

A planar-circular unbalanced magnetron was used as the plasma source for this investigation. A preliminary comparison study using High Power Impulse Magnetron Sputtering (HiPIMS) found good agreement between the diagnostics for electron density and temperature measurements up to $B = 33$ mT[23]. The aim of this research is to extend the comparison study to the lower-density DC magnetron mode and determine the plasma conditions for which unmagnetized Langmuir probe theory gives a reasonable indication of electron properties.

The following section, Sec. II, contains a description of the experimental apparatus, including the diagnostic systems, the data interpretation methods and an estimation of the measurement uncertainties. The results are presented in Sec. III and a discussion comparing the diagnostics follows in Sec. IV. Sec. V is the conclusion. It should be emphasized that the aim of this research is comparison of the two diagnostic techniques rather than investigating the discharge physics, and the content of the following sections reflects this.

II. EXPERIMENTAL SETUP

The experimental setup for Langmuir probe and Thomson scattering measurements during HiPIMS was described in an earlier publication[23]. In this section, the important aspects of the HiPIMS setup are detailed, along with the apparatus and procedures for the DC magnetron measurements.

A. Magnetron sputtering system

A VTech 150 series unbalanced magnetron (supplied by GENCOA Ltd) equipped with a 150 mm diameter planar tungsten target (purity >99.95%) was mounted vertically above the vacuum chamber, which was evacuated to a base pressure of $\sim 1.5 \times 10^{-3}$ Pa. The height of the target surface was adjustable with respect to the diagnostic alignment. Argon gas (>99.99% purity) was fed into the vacuum chamber using a mass flow controller and the chamber pressure was monitored using a capacitance manometer. The magnetron discharge was operated in two modes: a lower plasma density DC mode using a Pinnacle Plus power supply (Advanced Energy Inc.), and a higher density HiPIMS mode using a Sinex3 unit (Chemfilt AB Ltd). The target voltage during HiPIMS was measured using a x100 voltage probe (Tektronix P5100) and the discharge current was measured using a Pearson current monitor (model 110A). The current-voltage waveforms were recorded using the Tektronix DPO3034 oscilloscope.

Measurements were made in three regions of the discharge, denoted by $P1$, $P2$ and $P3$. The measurement positions in the radial-height plane (r-z) are shown in figure 1, and their azimuth locations are shown in figure 2(a); note that the magnetic field configuration is azimuthally symmetric. Position $P1$ is at the magnetic null ($r = 0$ mm, $z = 61.5$ mm) where $B \lesssim 1$ mT. Regions $P2$ and $P3$ are within the magnetic trap ($r = 41$ mm, $z = 10$-50 mm), where $B \approx 5-33$ mT, with B increasing as the target surface is approached (z decreasing). The azimuth angles of $P2$ and $P3$ are 225° and 315°, respectively (measured anticlockwise from laser entry through the center of the chamber); this changes the geometry of the scattering system with respect to the local magnetic field direction as described in the following section.

B. Thomson scattering system

A schematic plan view of the Thomson scattering apparatus is shown in figure 2(b); the chamber was designed to reduce the amount of stray laser light reaching the detector. A Nd:YAG laser operated at the second-harmonic wavelength, 532 nm, was the radiation source for the experiment. The laser supplied $\lesssim 240$ mJ per pulse, had a pulse duration of 5 ns, a beam divergence of 0.5 mrad and a 10 Hz repetition rate. The laser was focused by a 1 m focal length lens so that the beam diameter was ~ 0.25 mm at the measurement location. The beam path was in the plane of the target surface and the laser electric field was linearly polarized in the direction perpendicular to this plane. For the measurements at $P1$, the laser

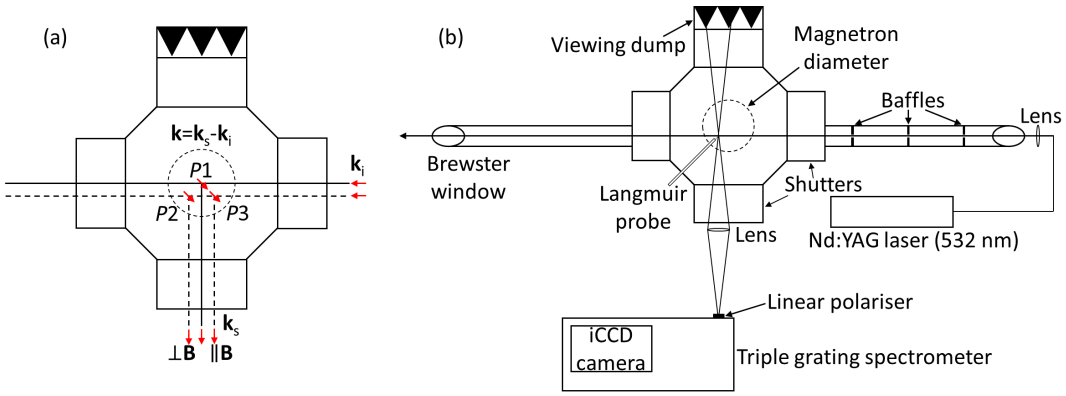

FIG. 2. (a) Azimuth location of the scattering volumes and the direction of the scattering wavevectors. (b) Schematic of the Thomson scattering apparatus. The viewing dump, Brewster windows, baffles and the notch filter in the triple grating spectrometer attenuate the stray laser light signal reaching the iCCD camera. The shutters on the chamber were closed when measurements were not being taken. A linear polarizer at the entrance to the spectrometer improves the signal to noise ratio by attenuating the unpolarized plasma emission signal.

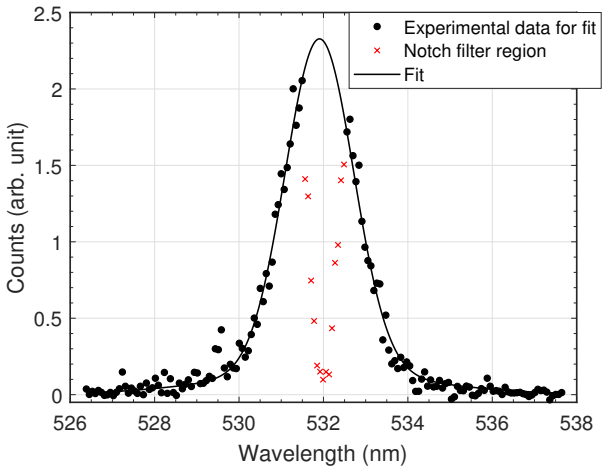

FIG. 3. Thomson scattering spectrum measured at $P2$ ($z = 20$ mm) from 6000 laser pulses for discharge conditions of 100 W DC and 1.6 Pa of argon gas. A double-Gaussian fit was applied to the region outside of the notch filter attenuation (531.5-532.5 nm). The electron density and temperature obtained for the two electron populations were (1.8×10^{17} m^{-3}, 0.6 eV) and (3.0×10^{16} m^{-3}, 6.2 eV), respectively.

beam passed through the center of the chamber, whereas for measurements at $P2$ and $P3$, the beam was offset by a perpendicular distance of 29 mm from the center of the chamber. The scattered light was collected by a lens (75 mm diameter, 200 mm focal length) positioned at 90° with respect to both the laser propagation and polarization directions. The direction of the scattering wavevectors are shown in figure 2(a): incident laser wavevector ($\mathbf{k}_i$), wavevector of the scattered radiation detected ($\mathbf{k}_s$), and the wavevector defined as $\mathbf{k}$=$\mathbf{k}_s$-$\mathbf{k}_i$. A Thomson scattering spectrum is proportional to the EVDF in the direction of $\mathbf{k}$[15]. This direction is constant for all measurements, however, its orientation is perpendicular and parallel to the local magnetic field for regions $P2$ and $P3$, respectively.

The scattered light was dispersed by a triple-grating spectrometer (Horiba T64000) which had an effective entrance slit of 0.30 mm × 6 mm. The spectrometer was configured in the double-subtractive configuration to attenuate the wavelength region 531.5-532.5 nm using a mask for removal of the stray light and Rayleigh scattering signals. An intensified charge-coupled device (iCCD) camera (Andor iStar) recorded the spectra and the measurements were averaged over the spatial dimension ($\lesssim 3$ mm). An example Thomson scattering spectrum is shown in figure 3. The wings of the Thomson spectra were fit with either a single or double-Gaussian curve, which corresponds to a single or bi-Maxwellian EVDF respectively, to obtain n_e and T_e. The criteria for accepting a double-Gaussian fit was that the $1/e$ amplitude values from the two Gaussian curves were at least twice the detector noise level, and the density from the single Gaussian fit was $< 95\%$ of the double-Gaussian fit. The system was calibrated for absolute density measurements using Rayleigh scattering from room temperature argon gas after each Thomson scattering measurement. Frequent calibration was required because the chamber window transmission decreased due to film growth during magnetron operation. The density overestimation due to the changing window transmission was $< 10\%$. The Thomson scattering signal was accumulated from 3000 to 9000 laser pulses during DC operation and 600 pulses during HiPIMS. For the time-resolved HiPIMS measurements (~ 5 μs resolution), the laser flashlamps were triggered by a transistor-transistor logic compatible signal derived from the target voltage waveform.

C. Langmuir probe system

1. *Apparatus*

The Langmuir probe stem was constructed from 6 mm outer diameter (OD) alumina tubing, which stepped down to OD=2 mm within the plasma. The probe was inserted radially into

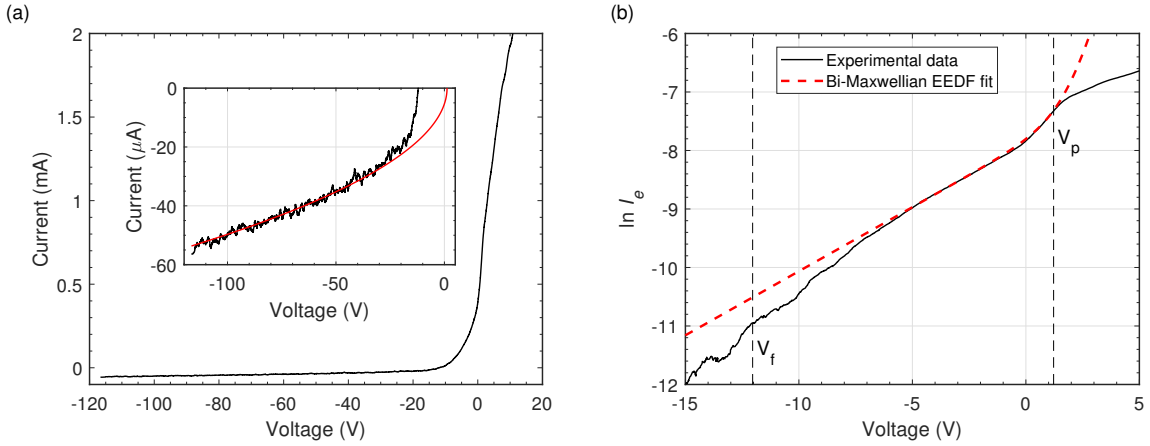

FIG. 4. (a) Langmuir probe current-voltage characteristic measured at $P1$ for discharge conditions of 100 W DC and an argon backing pressure of 1.6 Pa. The insert shows the ion current fit from Laframboise theory. (b) The fit to the electron current assuming a bi-Maxwellian EEDF.

the vacuum chamber in the target-surface plane. Tungsten wire with purity 99.95 % and radius $r_p = 50$ μm was fed through the alumina and exposed to the plasma to form the probe tip. An OD=1 mm alumina tube was recessed 2.5 mm from the plasma facing end of the OD=2 mm tube to ensure that the tungsten wire did not make contact with the sputter coated alumina. The probe tip used for the measurements at position $P1$ during DC operation was orientated parallel to the probe stem with length $l = 5.5$ mm. This is referred to as a 'straight' probe. The tips used in regions $P2$ and $P3$ were 'L' shaped with ~ 0.3 mm length parallel to the probe stem, which was neglected during analysis, and $l = 5$ mm length parallel to the target surface-normal. The 'L' probe was orientated so that the local magnetic field direction was approximately parallel to its surface-normal in order to reduce the effects of electron magnetization[5]. A 'L' probe ($r_p = 50$ μm, $l = 5.5$ mm) was also used for the HiPIMS measurements at $P1$. Several other probe tip dimensions were used in this study to investigate the effect of probe size on the electron density measurements. This is discussed in section III D.

To generate the probe IV characteristic during DC operation, a sawtooth voltage waveform was applied to the probe. The probe voltage was measured using a $\times 10$ voltage probe (Tektronix P6139A) at the base of the probe stem, and the current was calculated by measuring the voltage across a high-side 68.3 Ω resistor using the AD8479 precision difference amplifier. The waveforms were averaged over ≥ 50 cycles using an oscilloscope (Tektronix DPO3034), which was triggered by the voltage ramp, and the data was transferred to a personal computer for analysis. The IV characteristic was constructed using the MATLAB software package. An example curve is shown in figure 4(a). IV scans were routinely compared to check for increased probe surface area due to sputter coating.

The peak-to-peak voltage and DC offset of the sawtooth waveform were adjusted to limit the electron saturation current to the probe whilst acquiring the full ion saturation region (up to -120 V). The total period of the waveform was 325 ms with a duty cycle of 63%. During the off-time in the period, the probe potential was held constant at -120 V for ion bombardment cleaning. In addition, the probe was cleaned by biasing the probe into the electron saturation region so that the tungsten wire glowed before a set of measurements.

To acquire time-resolved HiPIMS probe measurements, a DC power supply was manually varied instead of the voltage ramp. In this case, the oscilloscope was triggered by the discharge voltage waveform, and the waveforms were averaged over 128 cycles before being recorded. The range of sense resistor was 1.5-500 Ω depending on the discharge conditions and whether collecting net ion or electron current. An analysis code using MATLAB constructed IV curves with < 1 μs resolution.

2. *Probe theory*

A review of probe theories can be found in various texts[2,3]. In this research, standard unmagnetized probe theories were used to interpret the IV characteristic, and these are summarized below:

- Plasma potential: the inflection point of the probe characteristic indicates V_p. It was located from the maximum in the first derivative of the probe characteristic.

- Electron temperature of a Maxwellian EEDF: this was calculated using

$$k_B T_e = e\left(\frac{d(\ln I_e)}{dV}\right)^{-1}, \tag{1}$$

for $V < V_p$, where k_B is the Boltzmann constant. The fit was applied to the voltage region near V_p. The electron current, I_e, was calculated by subtracting the ion current from the total probe current. The ion current was approximated by applying a fit of the form $[A(V_p - V)^{1/2} + B(V_p - V)]$, where A, B are fitting coefficients, to the region $V < V_f - 20$ V and then extrapolating to V_p.

- Electron density: this was calculated using

$$n_e = \frac{4I_{es}}{eA_p}\left(\frac{\pi m_e}{8k_B T_e}\right)^{1/2}, \quad (2)$$

where I_{es} is the electron (saturation) current at V_p, A_p is the probe area, e is the electron charge and m_e is the electron mass. This equation assumes that there is no sheath around the probe when it is biased at the plasma potential and collisionless electron collection, which requires $\lambda_e/r_p \gg 1$, where λ_e is the electron mean free path length. The peak cross-section for electron-argon neutral collisions[24] is $\sigma \sim 2\times10^{-19}$ m^2 between electron energies 0.12-10 eV, giving $\lambda_e/r_p \sim 164-881$ for the pressure range used in this study (0.47-2.53 Pa) with the $r_p = 50$ μm probe. When considering electron-argon ion Coulomb collisions (similar mean free path to electron-electron collisions)[25], the ratio is equal to $\lambda_e/r_p \sim 1602$ and ~ 298 for typical DC ($n_e \sim 10^{17}$ m^{-3}, $T_e \sim 0.5$ eV) and HiPIMS ($n_e \sim 5\times10^{18}$ m^{-3}, $T_e \sim 1.5$ eV) plasma conditions, respectively. Thus, in the absence of a magnetic field, collisionless electron collection would be justified for both modes, with the assumption more valid for the DC plasma conditions.

- Electron temperature and density of a bi-Maxwellian EEDF: this is apparent when there are two distinct gradients in the lnI_e against V plot; an example is shown in figure 4(b). The total current is

$$I_e = I_c \exp\left(\frac{e(V-V_p)}{k_B T_{c,P}}\right) + I_w \exp\left(\frac{e(V-V_p)}{k_B T_{w,P}}\right), \quad (3)$$

for $V \leqslant V_p$, where I_c and I_w are the saturation currents of the cold and warm populations, respectively; $T_{c,P}$ and $T_{w,P}$ are the cold and warm electron temperatures, respectively. Firstly, a fit to the warm electron current was performed and extrapolated to the plasma potential. This fit was then subtracted from the total electron current to leave only the cold component, which was then fitted. Equations 1 and 2 were used to calculate the electron temperature and density of the components.

- Three-dimensional EEDF for a non-Maxwellian plasma: the Druyvesteyn formula was implemented by numerical differentiation when the probe characteristic appeared neither Maxwellian or bi-Maxwellian. The first derivative of I_e against V was smoothed using a second-order Savitzky–Golay filter with window length 2 V prior to taking the second derivative. Integration of the EEDF gives the electron density, $n_{e,D}$, and the mean electron energy of the distribution defines an effective electron temperature, $T_{e,D}$=2<E>/3.

- Ion density: The plasma ion density is equal to the electron density through quasineutrality. The collisionless orbital-motion theory by Laframboise[26] was implemented using the parameterization by Chen[27] for zero ion temperature ($T_i = 0$) and $0 < r_p/\lambda_D < 100$. A fit to the region $V < V_f - 20$ was applied to the measured ion current by minimizing the sum of the squares of the residuals. The generation of theoretical curves in units of ampere required T_e, V_p, n_i and the probe tip dimensions. The plasma parameters were taken from the probe analysis described above, except for n_i, which was the fitting parameter.

The condition when orbital motion collection by the probe is impeded because of collisions is

$$\lambda_i < \lambda_{OML} \equiv r_p\left(\frac{e(V_p-V)}{k_B T_i}\right)^{1/2}, \quad (4)$$

where λ_i is the ion mean free path and λ_{OML} is a parameter derived from orbital motion limited theory[13], valid for $(r_p/\lambda_D < 3)$[2,3], therefore, DC mode only. Assuming an argon ion temperature of $T_i = 300$ K and $V_p - V = 100$ V, a value of $\lambda_{OML} = 3.1$ mm is obtained for the $r_p = 50$ μm probe. The cross-section for ion momentum exchange collisions with argon neutrals[28] is $\sigma \sim 1.5\times10^{-18}$ m^2, giving $\lambda_i = 1.1-5.9$ mm for the pressure range used in this study. In addition, the ion mean free path from Coulomb collisions, which is dominated by ion-ion collisions,[25] is of the order 1 mm when considering the typical DC plasma conditions. Since λ_i and λ_{OML} are comparable in magnitude, the probe operates in the weakly collisional regime where ion dynamics are a mixture of orbital and radial motion. This can increase the probe ion current compared to a strictly collisionless plasma, and hence, overestimate the ion density[9,13,14].

For the typical HiPIMS plasma conditions, OML theory is not valid since $r_p/\lambda_D > 3$, so it is instructive to compare values of λ_i/λ_D for the HiPIMS and DC modes to determine the relative degree of collisionality in the probe sheath. For both cases λ_i can be approximated by the argon ion-ion Coulomb collision mean free path[25], giving $\lambda_i/\lambda_D \sim 65$ and ~ 7 for the DC and HiPIMS conditions, respectively. Hence, the assumption of collisionless ion collection is more valid for the DC mode.

D. Measurement uncertainties

This section considers the magnitude of the experimental error in the measurements of plasma density and electron temperature made by each diagnostic in order to determine the accuracy of the diagnostic comparison.

Gating of the camera intensifier by the laser pulse and setting a high gain ensured that the main source of noise in a Thomson scattering spectrum were the fluctuations in the overlapping plasma emission spectrum rather than noise generated inside the iCCD camera. The quality of the Gaussian function fit to a Thomson scattering spectrum was affected by this noise level. Other sources of error include plasma drift during the integration time; measuring the laser power; measuring the chamber pressure during the Rayleigh scattering calibration; and the systematic electron density overestimation as a result of the window transmission being lower during

Section	Mode	Position	r_{ge}/r_p	r_{ge}/λ_D
III A	DC	$P1$	42-48	88-181
III B	DC	$P2$	2-9	6-33
III C	HiPIMS	$P1$	29-107	> 333

TABLE I. Summary of the electron magnetization parameters at different measurement positions and operating modes. Gyroradius was approximated by assuming that the gyration kinetic energy is 2/3 of the total (three-dimensional) kinetic energy. The total electron kinetic energy and Debye length were calculated using the Thomson scattering measurements.

the Rayleigh scattering calibration compared to the start of the Thomson scattering measurement. An estimate for the combined effect of the factors described above, except for the systematic window transmission error, was found by calculating the standard deviation of the plasma parameters from multiple measurements. The mean of the relative standard deviation for electron density and electron temperature measurements were $\sim 6\%$ and $\sim 8\%$, respectively. Taking into account a 10% upper limit for the systematic overestimation of electron density from the Rayleigh scattering calibration, a general upper limit for the electron density error was $\sim 16\%$.

The main sources of error for the Langmuir probe measurements were measuring the probe surface area; and noise on the *IV* characteristic, resulting in curve fitting errors, originating from plasma fluctuations and the probe circuitry. The combined effect of the error sources was estimated by performing repeat measurements using different probes which had similar lengths and equal radii. The mean of the relative standard deviation for the plasma density and electron temperature measurements was between $10-15\%$. Therefore, a reasonable upper limit for the general error in the plasma parameters determined by the probe was $\sim 15\%$.

The discussion above indicates that results from the two methods can be considered consistent if the values are within $\sim 20\%$ of each other. In Sec. III, when direct comparisons are made, the errors for those specific conditions are used.

III. RESULTS

This section is divided into four parts; three describing the measurements from different discharge conditions and locations (Sec. III A-C), and a final section describing the checks that were performed to confirm the reliability of the measurements from each diagnostic (Sec. III D). Table I summarizes the magnetron power supply, the measurement position and the electron magnetization parameters for Sec. III A-C. The electron magnetization parameters relate the electron gyroradius to the probe radius (r_{ge}/r_p) and the probe sheath length scale (r_{ge}/λ_D). The parameters tend to zero in the limit of strong B-field.

The error bars shown for the Thomson scattering measurements represent the standard deviation from $\geqslant 3$ repeated measurements. The repeatability of the probe parameters was generally within 15% during DC magnetron operation. Error bars, representing the standard deviation from 4 repeated measurements, were plotted for the probe measurements during HiPIMS because this threshold was exceeded in the afterglow period. Unless explicitly stated, the diagnostics were not operated simultaneously and the probe was not inside the vacuum chamber during the scattering measurements.

A. Negligible B-field, low-density

The measurements reported in this section were made at position $P1$, where the magnetic field strength is negligible, during DC operation. Power and pressure scans were performed: 15-125 W with 1.6 Pa of argon gas, and 0.47-2.53 Pa of argon gas at 25 W. Figures 5(a) and 6(a) show the electron temperature measurements made by both diagnostics from the respective scans. The Thomson scattering measurements were consistent with a Maxwellian distribution, whereas a bi-Maxwellian EEDF was obtained for most of the probe measurements. The cold electron temperature measured by the probe has good agreement with Thomson scattering (~ 0.45 eV). An exception is at 0.47 Pa, where the EEDF determined by the probe is Maxwellian with an electron temperature of $T_{e,P} = 4.8$ eV. This result was confirmed by taking repeat measurements using a 'straight' probe with dimensions of $r_p = 25$ μm, $l_p = 10$ mm. The cause of this discrepancy is discussed in section IV A.

The corresponding plasma density measurements are shown in figures 5(b) and 6(b). Plotted is the electron density determined from Thomson scattering using a Gaussian fit ($n_{e,T}$), and the electron ($n_{e,P}$) and ion ($n_{i,P}$) densities from the Langmuir probe. The results from the diagnostics show significant quantitative differences: $n_{e,T}$ is systematically above $n_{e,P}$ by up to an order of magnitude, and $n_{i,P}$ exceeds $n_{e,P}$ by a factor of ~ 3. The relative density of the cold and warm electron populations measured by the probe were $\sim 50\%$ (not shown).

B. Weak B-field, low-density

The measurements reported in this section were made at position $P2$, where electron magnetization is important, during DC operation. The discharge conditions were 100 W and 1.6 Pa of argon gas. Figure 7(a) shows the Langmuir probe and Thomson scattering electron temperature measurements as a function of distance from the target surface (z). The EVDF's determined from Thomson scattering between $z = 30-50$ mm were Maxwellian, characterized by an electron temperature <1 eV, but closer to the target there was evidence of an additional warm population of electrons. The criteria for a double-Gaussian fit (discussed in Sec. II B) were satisfied for some of the measurements at $z = 10$ and 20 mm, returning a warm electron temperature of $T_{w,T} \sim 5.5$ eV. The probe determined EEDF's were non-Maxwellian so the Druyvesteyn method was used to calculate an effective electron temperature, and this has good agreement with $T_{w,T}$.

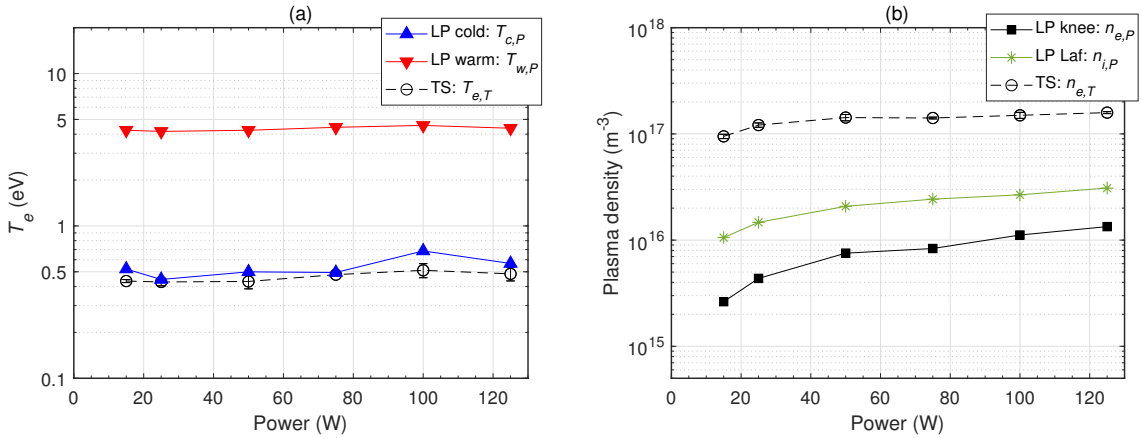

FIG. 5. Power dependence of (a) electron temperature and (b) plasma density measured by Langmuir probe and Thomson scattering during DC operation. The data analysis methods are indicated in the legend. The argon gas pressure was 1.6 Pa and the measurements were performed at position $P1$.

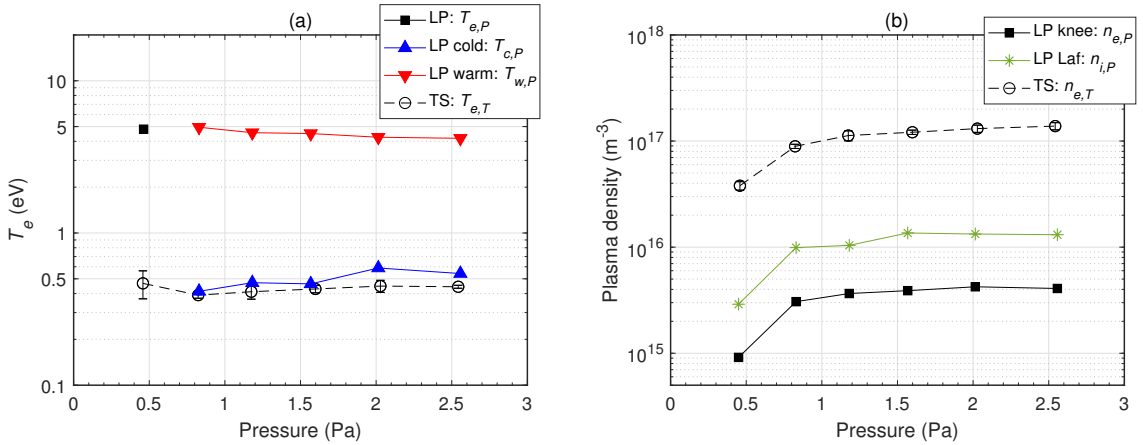

FIG. 6. Pressure dependence of (a) electron temperature and (b) plasma density measured by Langmuir probe and Thomson scattering during DC operation. The data analysis methods are indicated in the legend. The discharge power was 25 W and the measurements were performed at position $P1$.

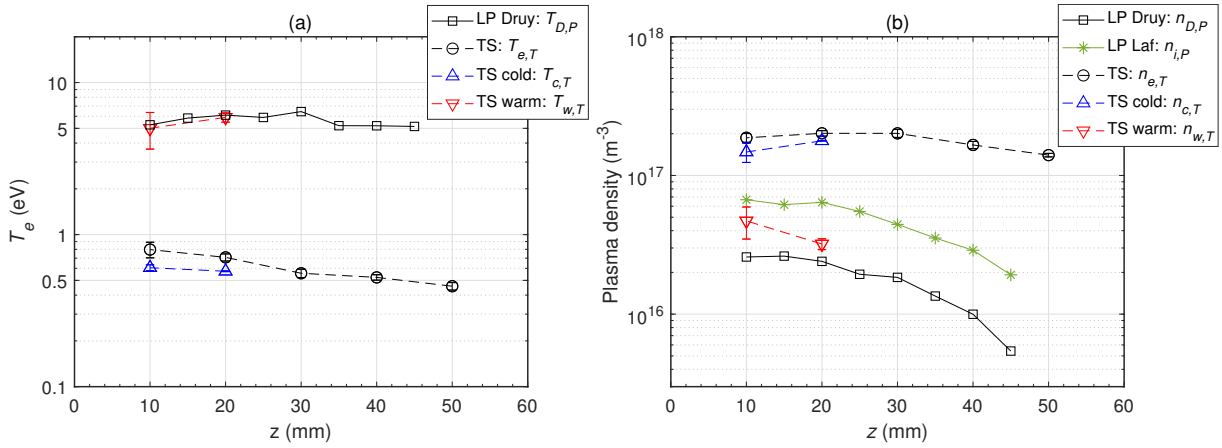

FIG. 7. (a) Electron temperature and (b) plasma density as a function of axial distance from the target measured by Langmuir probe and Thomson scattering during DC operation. The data analysis methods are indicated in the legend. The DC discharge power was 100 W, the argon gas pressure was 1.6 Pa and the measurements were performed in region $P2$. The magnetic field strength varied from 5 mT ($z = 50$ mm) to 33 mT ($z = 10$ mm).

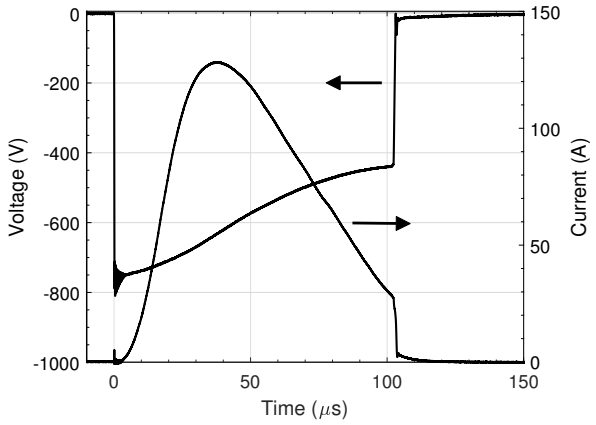

FIG. 8. Current-voltage waveforms of the HiPIMS discharge. The target voltage had a pulse width of 100 μs, a repetition rate of 50 Hz, a peak power per unit area of 450 Wcm^{-2} and the argon gas pressure was 1.6 Pa.

The corresponding plasma density measurements are shown in figure 7(b). Plotted is $n_{e,T}$; the cold ($n_{c,T}$) and warm ($n_{w,T}$) electron densities determined from Thomson scattering using a double-Gaussian fit; the electron density determined from the Druyvesteyn method ($n_{D,P}$); and $n_{i,P}$. The probe determined densities are significantly below $n_{e,T}$ and $n_{c,T}$, but they are comparable to $n_{w,T}$.

As aforementioned in Sec. II B, the Thomson scattering system was sensitive to the EVDF component perpendicular to the magnetic field at position $P2$. Measurements were also performed at position $P3$ ($z =$ 10-50 mm) in order to measure the component of the EVDF parallel to the magnetic field. Similar n_e and T_e were obtained at $P2$ and $P3$ for discharge conditions of 100 W and 1.6 Pa of argon gas, although, the Thomson scattering diagnostic detected a systematic difference in the drift velocities (not shown) by measuring the shift of the Gaussian peak from the laser wavelength. The maximum wavelength shift was 0.08 ± 0.03 nm; however, the maximum ratio of the drift velocity to the root mean square speed, calculated using T_e for a non-drifting one-dimensional distribution, was 0.1. Therefore, we conclude that the anisotropy in the target-surface plane is small.

C. Negligible B-field, high-density

The measurements reported in this section were made at position $P1$, where the magnetic field strength is negligible, during HiPIMS operation with 1.6 Pa of argon gas. Figure 8 shows the discharge voltage and current waveforms. The target voltage had a pulse width of 100 μs, a repetition rate of 50 Hz and a peak power per unit area of 450 Wcm^{-2} (normalized by the entire target area). A subset of these measurements have been presented elsewhere[23], but they are included here for completeness and ease of comparison with the measurements in the DC conditions.

Figure 9(a) shows the electron temperature from both diagnostics as a function of time from the start of the voltage pulse. A Gaussian fit was appropriate for the Thomson scattering measurements except at $t = 10$ μs when a double-Gaussian fit was applied. The properties of the two electron populations at $t = 10$ μs were $T_{c,T} = 0.8 \pm 0.2$ eV and $n_{c,T} = (6.7 \pm 1.9) \times 10^{17}$ m^{-3} for the cold group, and $T_{w,T} = 3.7 \pm 0.5$ eV and $n_{w,T} = (1.0 \pm 0.2) \times 10^{18}$ m^{-3} for the warm group. The probe data was consistent with a Maxwellian distribution throughout and has excellent agreement with Thomson scattering during the activeglow period, except the cold population of electrons at $t = 10$ μs was not detected. This was due to the IV characteristic being dominated by the warm population (not shown). During the afterglow period, the error in the probe determined electron temperature increased because the number of data points between the plasma and floating potentials for curve fitting decreased. The electron temperature determined by the probe is systematically a factor of ~ 1.5 greater than the Thomson scattering measurements, which approximately corresponds to the lower limit of the probe error bars.

Figure 9(b) shows the total plasma density from both diagnostics as a function of time. The probe ion density was calculated using the argon ion mass. This results in lower bounds because the contribution of tungsten ions to the probe ion current can be significant during HiPIMS. The upper bounds calculated using the tungsten ion mass (not shown) are a factor ~ 2.9 times greater than the lower bounds. Nevertheless, there is good agreement between the diagnostics (within a factor of ~ 1.5), using both electron and ion current theories, to calculate plasma density.

D. Diagnostic checks

The results presented in the previous sections show that the plasma density determined by the probe is significantly lower than the Thomson scattering measurements of electron density during DC operation. This section describes the background reliability checks that were performed to ensure that the data was obtained and analyzed correctly.

1. Thomson scattering

To confirm the reliability of the Thomson scattering measurements checks of laser perturbation, anomalous Mie scattering and the Rayleigh scattering calibration procedure were carried out. Firstly, the laser power was varied from 1.1 W to 2.4 W during separate Thomson scattering measurements using both magnetron power supplies, and the Thomson scattering spectra did not change. This gives confidence that photoionization and plasma heating by the laser is negligible. Secondly, scattering measurements without the spectrometer notch filter in place were performed to check for Mie scattering from the sputtered tungsten at the laser wavelength. The signal at the laser wavelength decreased by 15% when the plasma was on, for measurements at $P2$ ($z = 30$ mm) with discharge conditions of 50 W DC and 1.6 Pa of argon gas,

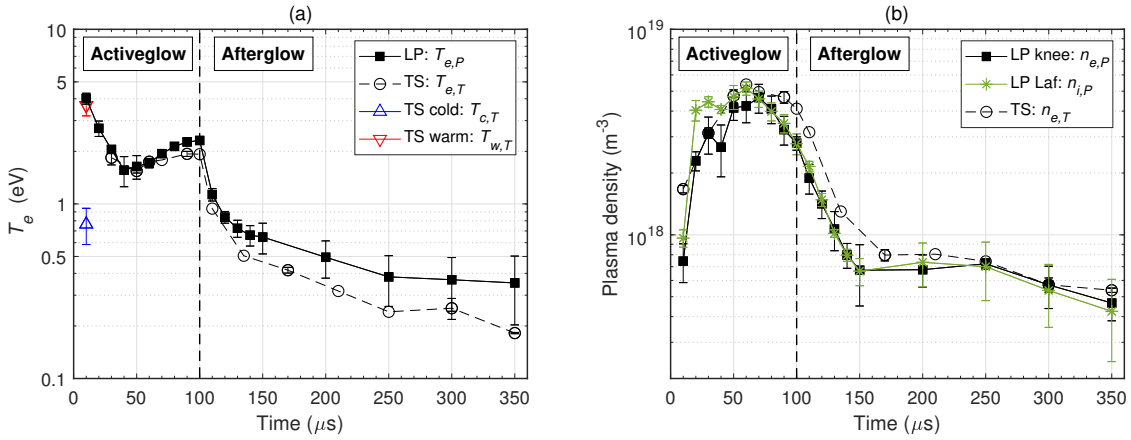

FIG. 9. Temporal profile of (a) electron temperature and (b) plasma density measured by Langmuir probe and Thomson scattering during HiPIMS at position $P1$. The data analysis methods are indicated in the legend. The target voltage had a pulse width of 100 μs, a repetition rate of 50 Hz, a peak power per unit area of 450 Wcm^{-2} and the argon gas pressure was 1.6 Pa.

compared to when there was just gas in the chamber. This rules out the possibility of misidentifying the Thomson scattering signal from an excessively large Mie scattering signal, and instead indicates gas rarefaction[29]. Finally, the Rayleigh scattering calibration procedure for absolute density measurements was extensively checked and verified by performing the calibration with nitrogen gas, varying the gas pressure range (and data accumulation time), varying the laser power at constant gas pressure, and using a second pressure gauge.

These checks confirmed that the reported Thomson scattering measurements were reproducible, reliable and accurate.

2. *Langmuir probe*

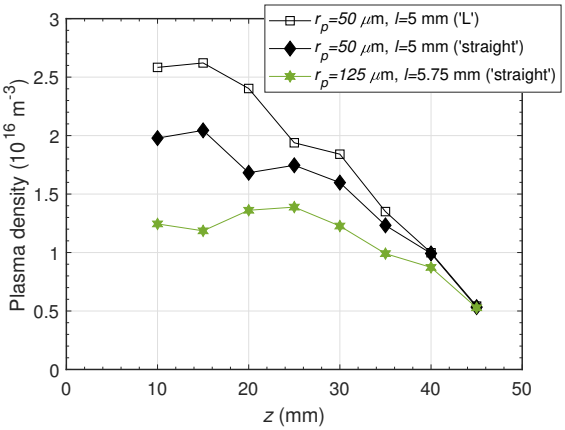

FIG. 10. Comparison of different probe sizes and orientations for electron density measurements as a function of axial distance from the target in region $P2$. Electron density was calculated using the Druyvesteyn method. The DC discharge power and argon gas pressure were 100 W and 1.6 Pa, respectively. The magnetic field strength varied from 6 mT ($z = 45$ mm) to 33 mT ($z = 10$ mm).

The main checks for the Langmuir probe included investigating the influence of electron magnetization on the collected electron current; the plasma perturbation induced by the presence of the probe stem and biasing the probe tip; and the effect of the floating alumina tube adjacent to the probe tip. These are described below.

A possibility is that the magnetic field was significantly reducing the electron current collected by the probe in DC mode, even far from the target, which resulted in electron density underestimation. When electron magnetization is significant, the electron density determined by a probe is strongly dependent on the probe tip radius and its alignment with respect to the B-field[5]. Therefore, the measurements reported in Sec. III B were repeated using two 'straight' probe tips with their axes aligned approximately parallel to the local B-field. Their dimensions were $r_p = 50$ μm, $l_p = 5$ mm and $r_p = 125$ μm, $l_p = 5.75$ mm, respectively. Figure 10 shows the electron density calculated using the Druyvesteyn method as a function of distance from the target for these probes and the 'L' probe from Sec. III B. There is excellent agreement between the three probes at $z = 45$ mm, where the magnetic field strength is ~ 6 mT, but the density measurements diverge as the target is approached. One can conclude from figure 10 that the electron density underestimation by the probe at position $P1$, where $B \lesssim 1$ mT, is not caused by an electron magnetization effect that is dependent on the probe tip radius or its orientation.

The global plasma perturbation induced by a Langmuir probe was examined by performing Thomson scattering measurements with a probe inserted close to the scattering volume. A 'L' shaped probe ($r_p = 50$ μm, $l_p = 6.5$ mm) was radially inserted into the vacuum chamber with its length parallel to the target surface-normal so that its radial presheath was directed towards the scattering volume. The closest approach of the probe wire to the scattering volume without stray light adversely affecting the Thomson scattering system was ~ 13 mm; the scattering volume was positioned outside of the probe sheath. The power scan measurements in Sec. III A were repeated using the Thomson scattering diagnostic with

various probe biases applied (-100 V, V_f, V_p+ 5 V) but the same electron properties were obtained as when the probe was not inside the chamber. We conclude that the probe perturbation is localized in the DC magnetron and/or the scattering volume was not located in the perturbed plasma region.

Another possibility is that the floating alumina tube adjacent to the probe tip was reducing the collected current by a shadowing effect and/or a sheath interaction effect. To check for this, the measurements in Sec. III A were repeated using a longer probe tip whilst maintaining an approximately constant probe surface area. Electron properties measured using a $r_p = 25$ μm, $l_p = 10$ mm 'straight' probe were in agreement with a $r_p = 50$ μm, $l_p = 5.5$ mm 'straight' probe to within 20%. Therefore, we conclude that the alumina tube adjacent to the probe tip did not significantly influence current collection.

Other checks were to vary the time period of the voltage ramp applied to the probe (10-325 ms); repeat the measurements in Sec. III A using a 'L' rather than a 'straight' probe; calculate the ion density using orbital-motion-limited theory[30], which uses the ion current gradient, rather than the parameterization of Laframboise theory; and calculate electron temperature, and hence electron density using equation 2, from the gradient of the *IV* characteristic in the vicinity of the floating potential, as described in Ryan *et al.*[23], for a non-Maxwellian EEDF in magnetized plasma rather than using the Druyvesteyn method (the electron temperature was reduced by a factor ~ 2.2 and electron density increased by a factor ~ 1.8 compared to the Druyvesteyn method). We can rule out these considerations as being responsible for the diagnostic discrepancy.

IV. DISCUSSION

The results show that the diagnostics gave large quantitative differences for plasma density measurements during the lower-density DC operation, whereas for HiPIMS, the density agreement was good. Furthermore, the EEDF agreement was poor except during HiPIMS. The EEDF and plasma density comparisons are discussed separately in further detail below.

A. EEDF comparison

An important point is that the diagnostics measure different components of the EEDF or equivalently EVDF. The Thomson scattering diagnostic is sensitive to one-dimension determined by the scattering geometry, whereas the electron current collected by the probe, in theory, depends only on the EEDF components in the axis-normal plane of the tungsten wire. The Thomson scattering measurements in regions *P*2 and *P*3 (Sec. III B) showed that there was no significant anisotropy of the EEDF caused by the magnetic field in the target-surface plane, therefore, we do not expect anisotropy at *P*1 where the *B*-field is weaker. Henceforth, we assume that the plasma is isotropic and this allows a direct comparison of the EEDF measurements once converted into the same spatial dimension; the EEDF measurements presented are three-dimensional.

Before discussing the EEDF measurements it is worth pointing out the limitations of each diagnostic. The maximum electron energy sampled by the Thomson scattering system is 14 eV based on the wavelength range measured, however, the signal to noise ratio degrades as energy increases. This is a consequence of the electron population density, hence the Thomson scattering signal, decreasing as energy increases. In contrast, a Langmuir probe can measure energies up to $\gtrsim V_p - V_f$ but the diagnostic has the following limitations: plasma potential uncertainty gives the electron energy axis an erroneous offset and this is most significant for the low-energy part of the EEDF; the accuracy of the ion subtraction procedure is critical for measuring the distribution tail; and the Druyvesteyn method for non-Maxwellian EEDF's requires the second derivative of the *IV* characteristic and this necessities smoothing of the experimental data. This can lead to an apparent depletion of the low-energy region[31].

The influence of the magnetic field on probe measurements at position *P*1 is expected to be small, therefore the diagnostic agreement should be good. However during DC operation at this position, the probe determined EEDF's were generally consistent with a bi-Maxwellian distribution, whereas the Thomson scattering diagnostic detected Maxwellian EEDF's. An example is shown in figure 11(a) for 100 W DC and an argon pressure of 1.6 Pa. The following is plotted: EEDF obtained from fitting equation 3 to the probe *IV* characteristic; EEDF calculated using the probe Druyvesteyn method; EEDF obtained from the Thomson scattering Gaussian fit; and the Thomson scattering detection limit for a bi-Maxwellian EEDF, which has a warm electron temperature equal to the value measured by the probe, and a cold electron population with properties determined from the single Gaussian fit. The data shows that the low energy part ($\lesssim 3.5$ eV) of the probe determined EEDF is significantly depleted compared to the Thomson scattering measurement. This is reflected in the different densities determined for each method. Nevertheless, the shape of the analytical fits in this region are similar because the electron temperature measurement of the cold population made by the Langmuir probe has good agreement (within a factor of 1.3) with the Thomson scattering measurement. The presence of the warm electron population detected by the probe, however, cannot be verified because its density is below the Thomson scattering double-Gaussian detection limit; this is the case for all the DC measurements at position *P*1.

It should be noted that low energy depletion of the EEDF determined by a Langmuir probe has been reported in a previous probe and Thomson scattering comparison study using an ICP discharge by Bowden *et al.*[18]. They found the effect to be more extreme at lower pressure. This is consistent with the observation reported in Sec. III A, where only the Thomson scattering diagnostic detected a cold population of electrons at the lowest argon backing pressure (discharge conditions of 25 W DC and 0.47 Pa). Bowden *et al.*[18] concluded that either the probe is measuring perturbed plasma due to the presence

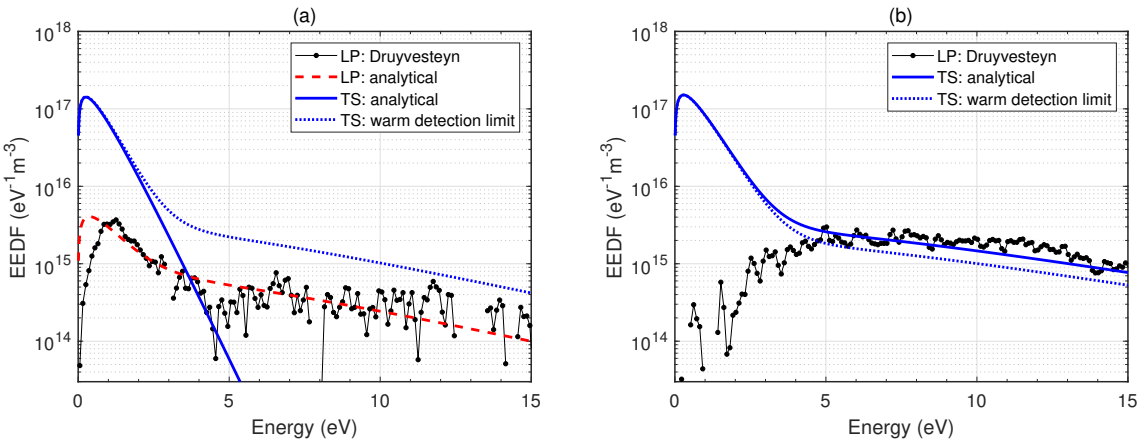

FIG. 11. Electron energy distribution function measurements made by Langmuir probe and Thomson scattering during DC operation at positions (a) $P1$ and (b) $P2$ ($z = 20$ mm). The data analysis methods are indicated in the legend. The discharge power and argon gas pressure were 100 W and 1.6 Pa, respectively.

of the probe or the Druyvesteyn method is not appropriate for measuring the low energy part of the EEDF. We speculate that the first conclusion is correct because the apparent depletion mechanism is more severe in the magnetron discharge, and this is consistent with the accepted idea that a probe inserted into a magnetized plasma is more perturbing compared to an unmagnetized environment[4]. Moreover, as discussed in Sec. III D 1, we cannot rule out the possibility of a significant plasma perturbation in the vicinity of the probe tip in the magnetron caused by the probe stem. It is also worth highlighting that a previous study using an ECR discharge[19] found that the shape of an EVDF determined by Thomson scattering was affected by the presence of a nearby probe stem and it caused the total scattering signal, and hence the electron density, to decrease. The scattering signal reduction by probe insertion was also observed in the ICP discharge but the shape of the EVDF did not change[18].

The results in Sec. III A,B show that the probe consistently measures an electron temperature or effective temperature with $T_e > 4$ eV. The corresponding electron densities are below the detection limit of the Thomson scattering diagnostic except at $z = 10$ and 20 mm during the region $P2$ measurements. Figure 11(b) compares the EEDF's from the diagnostics at $z = 20$ mm. Plotted is the EEDF calculated using the probe Druyvesteyn method; EEDF obtained from the Thomson scattering double-Gaussian fit; and the detection limit of the warm component measured by Thomson scattering as part of a double-Gaussian fit. There is good agreement between the diagnostics above 5 eV, but again, the low energy part of the probe EEDF is depleted. The depletion is more severe compared to the measurements at $P1$, but this is expected because the magnetic field is stronger (~ 21 mT compared to $\lesssim 1$ mT). The magnetic field impedes electron collection, so this effect is strongest for low energy electrons which have small gyroradii. Note that the speculated probe stem depletion mechanism may still be present at $P2$.

The HiPIMS measurements at position $P1$ from Sec. III C were discussed in a previous publication[23]. The electron property measurements, hence the EEDF's, from the diagnostics were consistent with one another. Therefore, depletion of the low energy electrons is not observed by the probe in HiPIMS unlike in the lower-density DC mode. This is discussed in the next section because significant low electron energy depletion results in total electron density underestimation.

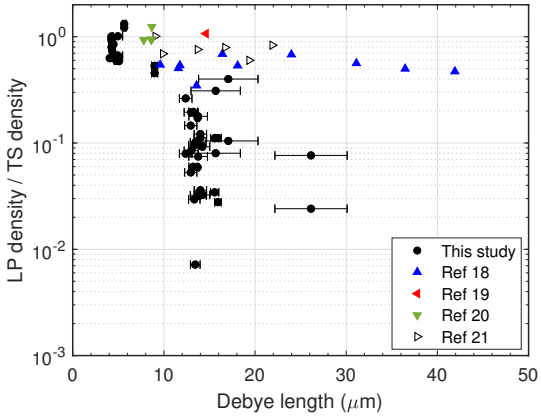

FIG. 12. Plasma density measured by Langmuir probe normalized by electron density determined from Thomson scattering as a function of Debye length (determined from Thomson scattering). Plotted is all data from Sec. III A-C and data from the literature[18–21].

B. Density comparison

In unmagnetized plasma it is common for probe measurements of ion density to exceed the electron density by up to an order of magnitude (e.g. Sudit and Woods[32] and therein) because of both ion-neutral collisional effects[9,13,14] and electron depletion as a result of drawing the relatively large electron saturation current from the plasma. However, it is surprising that the ion density measured by the probe is significantly

lower than the Thomson scattering measurement of electron density during DC mode because the effect of ion magnetization is expected to be small; the ion magnetization parameters during DC mode were $r_{gi}/r_p \geqslant 88$ and $r_{gi}/\lambda_D \geqslant 204$. Furthermore, as discussed in Sec. II C 2, the collisionless probe theories implemented are, to first order, more valid for the DC mode. In addition, the agreement between the diagnostics for electron density measurements improves as the magnetic field strength increases during the region *P*2 measurements, opposite to what is expected. These anomalous observations suggest that the probe perturbation is significant and dependent on the plasma conditions local to the measurement position.

One would expect the probe perturbation to be reduced in plasmas with small λ_D because the spatial extend of the sheath surrounding the floating stem and biased wire is smaller. Figure 12 shows that the diagnostic density agreement improves as λ_D decreases. Plotted is all data from Sec. III A-C; the graph axes are electron and ion density from the Langmuir probe normalized by the electron density from Thomson scattering, against the Debye length determined from Thomson scattering. In addition, data from several other comparison studies using different types of magnetized[19,20] and unmagnetized[18,21] discharges is included on the plot; the plasma density range from these references is $1.7-34\times10^{17}$ m^{-3}. It is common for the Langmuir probe to underestimate the plasma density by a factor of $\lesssim 2$, but the underestimation can be over an order of magnitude for the magnetron when $\lambda_D > 10$ μm, which corresponds to the DC mode. It is clear that the current collected by a probe is strongly influenced by the discharge physics.

The plasma replenishment rate is another important factor for determining the scale of the plasma perturbation induced by a probe. The floating probe stem and biased tungsten wire both deplete the plasma of charge, which has to be resupplied by ionization and then transported to the depleted region. The discharge physics of HiPIMS and DC mode is significantly different and this will affect the replenishment rate. Examples include: electrons gain more energy from sheath acceleration during the on-time of HiPIMS so each secondary electron can have more ionizing collisions before being lost; HiPIMS discharges have faster electron cross-field transport than DC discharges[33], therefore, electrons can more readily escape the main ionization zone of the discharge; the dense HiPIMS plasma has a high degree of target-metal ionization; HiPIMS has a greater gas rarefaction effect in front of the target; Coulomb collisions are more important during HiPIMS due to the higher plasma density; and the HiPIMS waveforms in this study did not reach steady-state.

V. CONCLUSION

The aim of this research was to assess the reliability of a Langmuir probe for electron property measurements in a weakly magnetized plasma environment, by comparing results obtained from the probe with laser Thomson scattering measurements. Thomson scattering was chosen as the benchmark technique because it provides absolute electron density measurements and it is insensitive to magnetic field effects. A magnetron was used as the plasma source due to its ability to operate in different discharge regimes (by changing the power supply) which cover a wide plasma density range.

Measurements were performed at different locations within the magnetic field configuration of the magnetron: at the magnetic null position where magnetic field effects on the probe measurement should be negligible, and within the last closed flux surface boundary at field strengths up to ~ 33 mT. The magnetron was operated in a DC mode, which provided densities of 4-20 $\times 10^{16}$ m^{-3}, and in a high-power pulsed-DC mode (HiPIMS), which provided densities in excess of 10^{18} m^{-3}. During DC operation, the bulk electron temperature was < 1 eV, but close to the target, the Thomson scattering diagnostic resolved a hot electron population ~ 5.5 eV. The HiPIMS discharge had a peak electron temperature at the start of the pulse ~ 3.7 eV, which decayed to ~ 0.2 eV after 250 μs into the pulse-off period.

We would expect the diagnostics to generate similar results in conditions for which unmagnetized probe theory is valid, regardless of the operating regime of the magnetron. However, there was agreement (within a factor of ~ 1.5) only for density measurements at the magnetic null for the higher-density HiPIMS mode. The electron densities determined by Thomson scattering during DC mode were an order of magnitude greater than the plasma density determined from the Langmuir probe, using both electron and ion collection theories, for certain discharge conditions.

The comparison of EEDF's was generally limited to the bulk electrons because the Thomson scattering diagnostic is insensitive to the tail of the distribution. When the conditions for unmagnetized probe theory were satisfied, the probe gave a reliable indication of the bulk electron temperature (within a factor of ~ 1.5) during both operating regimes. However, for the DC mode, the population density of the low energy part of the probe EEDF was depleted. This effect was more pronounced for measurements at locations with higher magnetic field strengths.

The reason for the discrepancy in plasma density measurements was investigated by carefully checking for perturbing effects from both diagnostics. The reliability of the Thomson scattering system was checked by considering laser intensity effects; investigating enhanced scattering due to other species; and the Rayleigh scattering calibration procedure was verified. The diagnostic was confirmed to be reliable. The reliability of the probe diagnostic was checked by repeating measurements with different probe tip dimensions and orientations in order to assess the plasma perturbation caused by the probe tip and the shadowing effect of the ceramic stem. These effects were not responsible for the diagnostic discrepancy. Any global effects were checked by simultaneous measurement of the two diagnostics, but the probe did not show any clear perturbation. However, the distance between the probe and scattering volume was limited by stray light levels, so the scattering volume may have been positioned outside of the perturbed region.

The conclusion from this study is that the presence of the probe stem in the discharge environment, intruding across

the magnetic field lines from the probe port to the measurement position, affects the development of the DC magnetron plasma. This effect is not seen in the HiPIMS case for an unknown reason that may be linked to its shorter Debye length-scale and the discharge physics in this highly transient pulsed regime. While the link between probe presence and perturbation in the DC case is not clear, elimination of other possible perturbative effects means that this is the only possible conclusion.

It is desirable to know the reasons for the discrepancies reported in this study because Langmuir probes are the most commonly used diagnostic in low temperature plasmas for electron property measurements, therefore, understanding their limitations is of paramount importance. It may be the case that the significant discrepancies are due to the specific nature of the magnetron discharge. It has a highly non-uniform magnetic field that changes in direction and intensity across small distances, and this might exacerbate the perturbing effect of any solid object inserted into the environment. Further investigations could include a similar study using a discharge with a more uniform field structure, and in which the density can be varied over a wide range without changing the plasma generation technique.

ACKNOWLEDGMENTS

This work was supported by the Engineering and Physical Sciences Research Council [EP/L01663X/1].

[1] V. A. Godyak, R. B. Piejak, and B. M. Alexandrovich, Journal of Applied Physics **73**, 3657 (1993).
[2] J. D. Swift and M. J. R. Schwar, *Electrical Probes for Plasma Diagnostics* (Iliffe Books LTD, London, 1970).
[3] P. M. Chung, L. Talbot, and K. J. Touryan, *Electric probes in stationary and flowing plasmas: theory and application* (Springer-Verlag, New York, 1975).
[4] D. Bohm, E. H. S. Burhop, and H. S. W. Massey, *The Characteristics of Electrical Discharges in Magnetic Fields*, edited by A. Guthrie and R. K. Wakerling (McGraw-Hill, New York, 1949).
[5] J. G. Laframboise and J. Rubinstein, Physics of Fluids **19**, 1900 (1976).
[6] E. Passoth, P. Kudrna, C. Csambal, J. F. Behnke, M. Tichý, and V. Helbig, Journal of Physics D: Applied Physics **30**, 1763 (1997).
[7] M. Usoltceva, E. Faudot, S. Devaux, S. Heuraux, J. Ledig, G. V. Zadvitskiy, R. Ochoukov, K. Crombé, and J.-M. Noterdaeme, Physics of Plasmas **25**, 063518 (2018).
[8] A. Simon, Physical Review **98**, 317 (1955).
[9] M. Tichy, P. Kudrna, J. Behnke, C. Csambal, and S. Klagge, Journal de Physique IV Colloque **7**, C4–397 (1997).
[10] P. Kudrna and E. Passoth, Contributions to Plasma Physics **37**, 417 (1997).
[11] I. G. Brown, A. B. Compher, and W. B. Kunkel, Physics of Fluids **14**, 1377 (1971).
[12] J. A. Tagle, P. C. Stangeby, and S. K. Erents, Plasma Physics and Controlled Fusion **29**, 297 (1987).
[13] B. M. Annaratone, M. W. Allen, and J. E. Allen, Journal of Physics D: Applied Physics **25**, 417 (1992).
[14] P. Bryant, A. Dyson, and J. E. Allen, Journal of Physics D: Applied Physics **34**, 1491 (2001).
[15] M. J. Van de Sande, *Laser scattering on low temperature plasmas*, Ph.D. thesis, Eindhoven University of Technology (2002).
[16] M. Usoltceva, E. Faudot, J. Ledig, S. Devaux, S. Heuraux, G. Zadvitskiy, R. Ochoukov, J. Moritz, K. Crombé, and J.-M. Noterdaeme, Review of Scientific Instruments **89**, 10J124 (2018).
[17] U. Fantz, Plasma Sources Science and Technology **15**, S137 (2006).
[18] M. D. Bowden, M. Kogano, Y. Suetome, T. Hori, K. Uchino, and K. Muraoka, Journal of Vacuum Science & Technology A **17**, 493 (1999).
[19] M. D. Bowden, F. Kimura, H. Muta, K. Uchino, K. Muraoka, and M. Maeda, Journal of Vacuum Science & Technology A **11**, 2893 (1993).
[20] S. Maurmann, V. A. Kadetov, A. A. I. Khalil, H.-J. Kunze, and U. Czarnetzki, Journal of Physics D: Applied Physics **37**, 2677 (2004).
[21] M. Noguchi, T. Hirao, M. Shindo, K. Sakurauchi, Y. Yamagata, K. Uchino, Y. Kawai, and K. Muraoka, Plasma Sources Science and Technology **12**, 403 (2003).
[22] S. A. Moshkalyov, C. Thompson, T. Morrow, and W. G. Graham, Journal of Vacuum Science & Technology A **18**, 1395 (2000).
[23] P. J. Ryan, J. W. Bradley, and M. D. Bowden, Physics of Plasmas **26**, 040702 (2019).
[24] S. J. Buckman and B. Lohmann, Journal of Physics B: Atomic and Molecular Physics **19**, 2547 (1986).
[25] M. A. Lieberman and A. J. Lichtenberg, *Principles of Plasma Discharges and Materials Processing*, 2nd ed. (John Wiley & Sons, Inc., Hoboken, 2005) p. 58.
[26] J. G. Laframboise, "Theory of spherical and cylindrical langmuir probes in a collisionless, maxwellian plasma at rest," Tech. Rep. UTIAS Report No. 100 (University of Toronto, 1966).
[27] F. F. Chen, Physics of Plasmas **8**, 3029 (2001).
[28] A. V. Phelps, Journal of Physical and Chemical Reference Data **20**, 557 (1991).
[29] S. M. Rossnagel, Journal of Vacuum Science & Technology A **6**, 19 (1988).
[30] H. M. Mott-Smith and I. Langmuir, Physical Review **28**, 727 (1926).
[31] F. Magnus and J. T. Gudmundsson, Review of Scientific Instruments **79**, 073503 (2008).
[32] I. D. Sudit and R. C. Woods, Journal of Applied Physics **76**, 4488 (1994).
[33] J. T. Gudmundsson, N. Brenning, D. Lundin, and U. Helmersson, Journal of Vacuum Science & Technology A **30**, 030801 (2012).